LAWRENCE
LIVERMORE
NATIONAL
LABORATORY

LLNL-CONF-420244

Turbulent Combustion in SDF Explosions

A. L. Kuhl, J. B. Bell, V. E. Beckner

November 13, 2009

JANNAF
SAN DIEGO, CA, United States
December 7, 2009 through December 11, 2009

Disclaimer

TURBULENT COMBUSTION IN SDF EXPLOSIONS

A.L. Kuhl[1], J.B. Bell[2], and V. E. Beckner[2]
[1]Lawrence Livermore National Laboratory
Livermore, California
[2]Lawrence Berkeley National Laboratory
Berkeley, California, USA 94551

ABSTRACT

A heterogeneous continuum model is proposed to describe the dispersion and combustion of an aluminum particle cloud in an explosion. It combines the gas-dynamic conservation laws for the gas phase with a continuum model for the dispersed phase, as formulated by Nigmatulin. Inter-phase mass, momentum and energy exchange are prescribed by phenomenological models. It incorporates a combustion model based on the mass conservation laws for fuel, air and products; source/sink terms are treated in the fast-chemistry limit appropriate for such gasdynamic fields, along with a model for mass transfer from the particle phase to the gas. The model takes into account both the afterburning of the detonation products of the C-4 booster with air, and the combustion of the Al particles with air. The model equations were integrated by high-order Godunov schemes for both the gas and particle phases. Numerical simulations of the explosion fields from 1.5-g Shock-Dispersed-Fuel (SDF) charge in a 6.6 liter calorimeter were used to validate the combustion model. Then the model was applied to 10-kg Al-SDF explosions in a an unconfined height-of-burst explosion. Computed pressure histories are compared with measured waveforms. Differences are caused by physical-chemical kinetic effects of particle combustion which induce ignition delays in the initial reactive blast wave and quenching of reactions at late times. Current simulations give initial insights into such modeling issues.

INTRODUCTION

We model experiments of Shock-Dispersed-Fuel (SDF) explosions in various chambers. The SDF charge consisted of 0.5-g spherical PETN booster surrounded by a paper cylinder (Fig. 1); the void volume of 1.6 cc was filled with 1-g of flake Aluminum (Fig. 2) with a bulk density of 0.604 g/cc. The charge was placed at the center of a barometric calorimeter (Fig. 3), a right circular cylinder of the following dimensions:

Calorimeter A: $L = 21\,cm,\ D = 20\,cm,\ L/D = 1.05,\ V = 6.6\ liters$

Calorimeter B: $L = 30\,cm,\ D = 30\,cm,\ L/D = 1.0,\ V = 21.2\ liters$

Calorimeter C: $L = 37.9\,cm,\ D = 36.9\,cm,\ L/D = 1.03,\ V = 40.5\ liters$

Detonation of the booster charge created a blast wave that dispersed the Al powder and ignited the ensuing Al-air mixture—thereby forming a two-phase combustion cloud embedded in the explosion. Afterburning of the booster detonation products with air also enhanced and promoted the Al-air combustion process. The main diagnostics consisted of eight Kistler 603B piezo-electric pressure gages located at *r* = 5 cm, 7.5 cm, 10 cm, 12.5 cm, and 15 cm on the lid of the chamber. Two atmospheres were used: (*i*) air—to investigate turbulent combustion of explosion products with air; and (*ii*) nitrogen—to evaluate mass fraction of HE detonated in small charges. A description of this barometric calorimeter technique can be found in [1]. Details of the parametric experiments with Al-SDF charges and with TNT charges are described by Kuhl and Reichenbach [2]. The historical development of the SDF charge concept may be found in [3-7]. An analytic solution to the problem of turbulent combustion of detonation products in a chamber has been found by Kuhl [8].

This work was performed under the auspices of the U. S. Department of Energy by Lawrence Livermore National Laboratory under Contract No. DE-AC52-07NA27344. It was sponsored by the Defense Threat Reduction Agency under IACRO # 06-40731 and IACRO # 09-4509I.

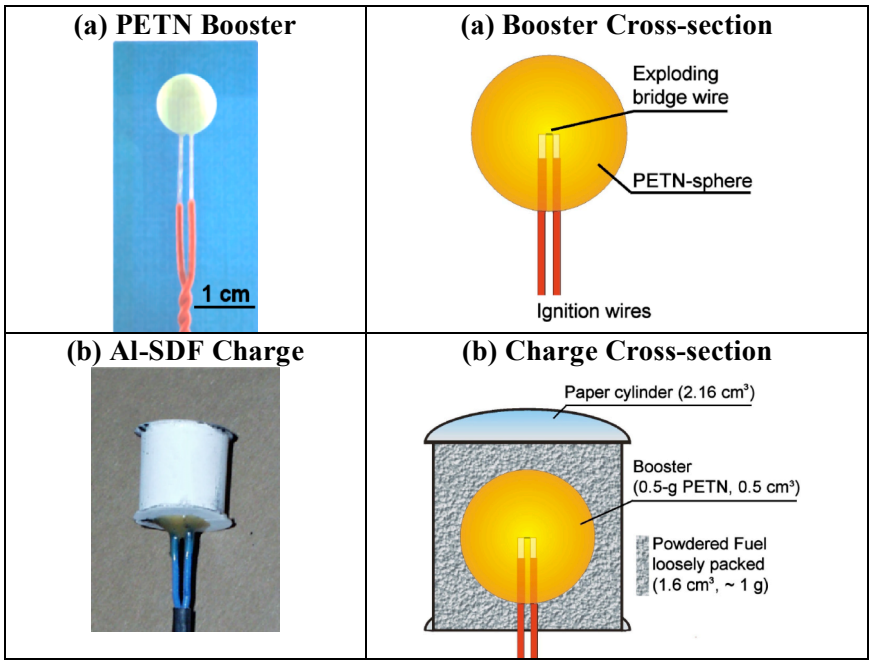

Figure 1. Charge construction: (a) 0.5-g PETN booster; (b) Al-SDF charge: booster plus 1-g Aluminum powder.

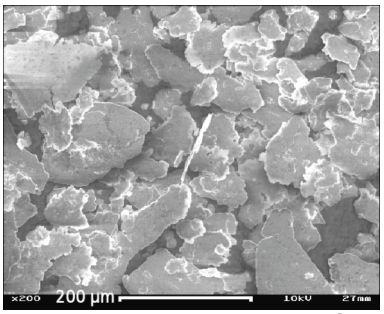

Fig. 2. SEM photograph of the flake Aluminum powder (Merck, AG).

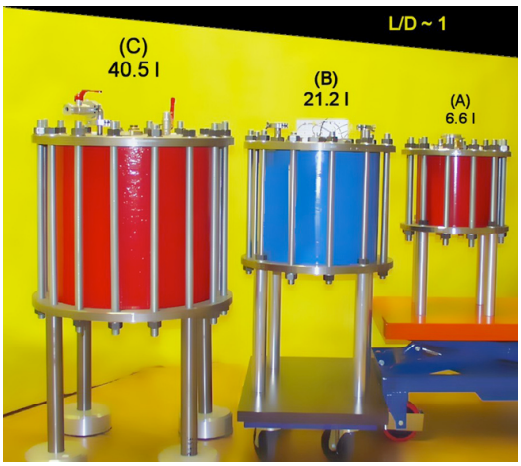

Fig. 3. Calorimeters: *A* (*V*=6.6 liters: *L*=21 cm, *D*=20 cm, *L/D*=1.05), *B* (*V*=21.2 liters: *L*=30 cm, *D*=30 cm, *L/D*=1.00) and *C* (*V*=40.5 liters: *L*=37.9 cm, *D*=36.9 cm, *L/D*=1.03).

Presented here is a two-phase model of the explosion/combustion process. It is based on gasdynamic conservation laws for the gas phase and the dilute continuum conservation laws for the particle phase as formulated by Nigmatulin [9]. Afterburning of the booster detonation products with air, and combustion of the fuel with air are both taken into account in the combustion model [10]. These model equations are integrated with an adaptive mesh refinement (AMR) code to describe the evolution of mixing and combustion in explosions [11].

MODEL

CONSERVATION LAWS

The model is based on the Eulerian multi-phase conservation laws for a dilute heterogeneous continuum as formulated by Nigmatulin [9]. We model the evolution of the gas phase combustion fields in the limit of large Reynolds and Peclet numbers, where effects of molecular diffusion and heat conduction are negligible on the gasdynamic fields. The flow field is governed by the following conservation laws:

Mass:
$$\partial_t \rho + \nabla \cdot (\rho \mathbf{u}) = \dot{\sigma}_s \tag{1}$$

Momentum:
$$\partial_t \rho \mathbf{u} + \nabla \cdot (\rho \mathbf{u}\mathbf{u} + p) = \dot{\sigma}_s \mathbf{v} - \dot{f}_s \tag{2}$$

Energy:
$$\partial_t \rho E + \nabla \cdot (\rho \mathbf{u} E + p\mathbf{u}) = -\dot{q}_s + \dot{\sigma}_s E_s - \dot{f}_s \cdot \mathbf{v} \tag{3}$$

where ρ, p, u represent the gas density, pressure and specific internal energy, $\mathbf{u}$ is the gas velocity vector, and $E \equiv u + \mathbf{u} \cdot \mathbf{u}/2$ denotes the total energy of the gas phase. Source terms on the right hand side take into account: mass transfer from the particle phase to gas phase ($\dot{\sigma}_s$), acceleration of particle phase by drag ($\dot{f}_s$), and heat exchange ($\dot{q}_s$) to the particle phase.

We treat the particle phase as an Eulerian continuum field. We consider the dilute limit, devoid of particle-particle interactions, so that the pressure and sound speed of the particle phase are zero. We model the evolution of particle phase mass, momentum and energy fields by the conservation laws of continuum mechanics for heterogeneous media [9]:

Mass:
$$\partial_t \sigma + \nabla \cdot \sigma \mathbf{v} = -\dot{\sigma}_s \tag{4}$$

Momentum:
$$\partial_t \sigma \mathbf{v} + \nabla \cdot \sigma \mathbf{v}\mathbf{v} = -\dot{\sigma}_s \mathbf{v} + \dot{f}_s \tag{5}$$

Energy:
$$\partial_t \sigma e_s + \nabla \cdot \sigma e_s \mathbf{v} = \dot{q}_s - \dot{\sigma}_s e_s \tag{6}$$

where σ and $\mathbf{v}$ represent the particle-phase density and velocity, and $e_s \equiv C_s T_s$ denotes the specific internal energy of the particle phase.

INTERACTIONS

The inter-phase interaction terms for mass, momentum, heat and particle burning take the form as described in Khasainov et al. [12]:

Mass Exchange:
$$\dot{\sigma}_s = \begin{cases} 0 & T_s < T_L \\ -3\sigma(1 + 0.276\sqrt{Re_s})/t_s & T_s \geq T_L \end{cases} \tag{7}$$

Momentum Exchange:
$$\dot{f}_s = \frac{3}{4}\frac{\rho}{\rho_s}\frac{\sigma}{d_s} C_D (\mathbf{u} - \mathbf{v})|\mathbf{u} - \mathbf{v}| \tag{8}$$

where $C_D = 24/Re_s + 4.4/\sqrt{Re_s} + 0.42$ and $Re_s = \rho d_s |\mathbf{u} - \mathbf{v}|/\mu$ (9)

Heat Exchange:
$$\dot{q}_s = \frac{6\sigma}{\rho_s d_s}\left[\frac{Nu\lambda(T - T_s)}{d_s} + \varepsilon\sigma_{Boltz}(T^4 - T_s^4)\right] \tag{10}$$

where $Nu = 2 + 0.6\,\mathrm{Pr}\sqrt{\mathrm{Re}_s}$ and $Pr = C_p\mu/k$ (11)

Ingignoli [13] Relation:
$$t_s = Kd_s^2 \tag{12}$$

where $K = 150\ \mathrm{s/cm}^2$. Transport properties for the various gases are listed in Appendix A. Previously, the above interaction terms (7)-(12) where used successfully by Veyssiere and Khasainov [14] to model steady, plane, double-front detonations in gaseous explosive mixtures containing suspended Al particles. In the current implementation, we convert the Al particles to a liquid at $T_L = 932\,K$. We assume that once in the liquid phase, the droplets quickly form a micro-mist due to intense accelerations by the gas phase—as has been demonstrated by Kobiera et al [15] for hexane droplets. At this point the liquid is assumed to be in velocity and temperature equilibrium with the gas phase, and we assume that the micro-mist is susceptible to diffusive combustion (limited by the oxidizer supply rate) without having to reach the vaporization temperature of Al (~2,300 K). Thus we treat the liquid as a fuel suitable for oxidation by the gas phase at a rate consistent with (7) and (12).

COMBUSTION

We consider two fuels: PETN detonation products[1] (F_1) and Aluminum (F_2), along with their corresponding combustion products: PETN-air (P_1) and Al-air (P_2). We model the global combustion of both fuels F_k with air (A) producing equilibrium combustion products P_k:

$$F_k + A \Rightarrow P_k \qquad (k = 1 \text{ or } 2) \tag{13}$$

The mass fractions Y_k of the components are governed by the component conservation laws:

Fuel-k:
$$\partial_t \rho Y_{Fk} + \nabla\cdot\rho Y_{Fk}\mathbf{u} = -\dot{s}_k + \delta_{k2}\dot{\sigma}_k \tag{14}$$

Air:
$$\partial_t \rho Y_A + \nabla\cdot\rho Y_A\mathbf{u} = -\sum_k \alpha_k \dot{s}_k \tag{15}$$

Products-k:
$$\partial_t \rho Y_{Pk} + \nabla\cdot\rho Y_{Pk}\mathbf{u} = \sum_k (1+\alpha_k)\dot{s}_k \tag{16}$$

Fuel and air are consumed in stoichiometric proportions: $\alpha_k = A/F_k$. In the above, $\dot{s}_k$ represents the global kinetics sink term. In this work we use the fast-chemistry limit that is consistent with the inviscid gasdynamic model (1)-(3), so whenever fuel and air enter a computational cell, they are consumed in one time step[2]. The term $\delta_{k2}\dot{\sigma}_k$ represents the conversion of Al from the particle phase to the gas phase, which creates a source of Al fuel.

EQUATIONS OF STATE

Our code carries the mixture density and specific internal energy, along with the gas composition in each cell. These are used to calculate the pressure and temperature in a computational cell based on

[1] Composition (in moles/kg) of expanded detonation products are: H_2O (11.5), CO_2 (10.65) and N_2 (6.31), along with CO (5.15) and H_2 (1.1) which serve as the fuel to be oxidized.

[2] Limitations of the fast-chemistry model are explored in the Discussion section.

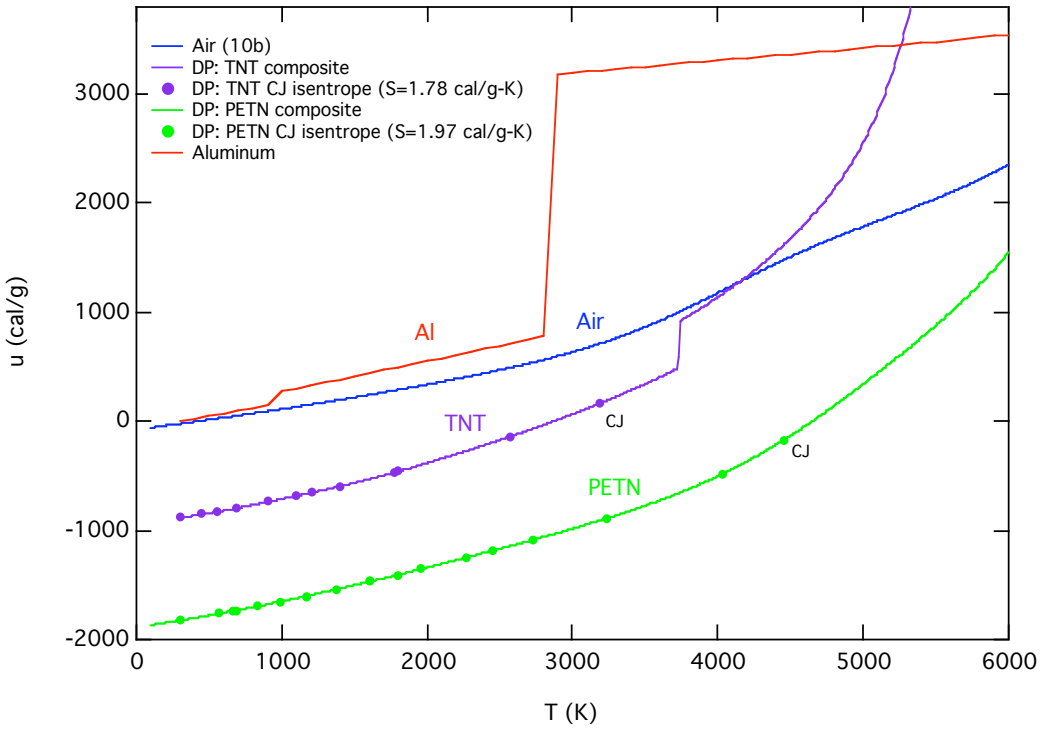

Figure 4. Loci of frozen Reactants states for SDF explosions; components of Air, Al, and PETN detonation products are shown in the specific internal energy-temperature plane.

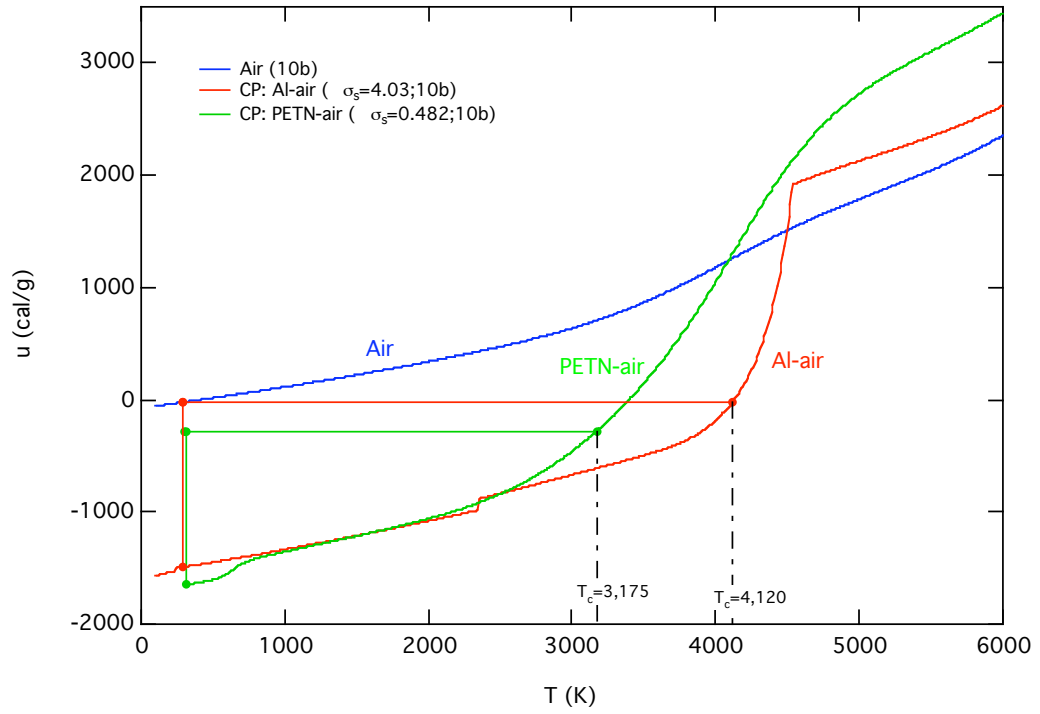

Figure 5. Loci of equilibrium Products states for SDF explosions; components of stoichiometric PETN-air afterburning and stoichiometric Al-air combustion are shown in the specific internal energy-temperature plane.

Equations of State (EOS). The thermodynamic states encountered during SDF explosions have been analyzed in [16]. Here we summarize only the salient features needed for the numerical modeling.

Figures 3 and 4 present the locus of states in the Le Chatelier diagram of specific internal energy versus temperature ($u-T$). Presented in Fig. 3 are curves for reactant components: PETN detonation products (DP), aluminum (Al) and air (A); their corresponding equilibrium combustion products (P_k) are depicted in Fig. 4. In this formulation, combustion becomes:

material transformations from Reactants → Products at constant energy

resulting in combustion temperatures of 3,175 K and 4,120 K for PETN-air and Al-air systems, respectively (see Fig. 4). The system is ***iso-energetic***—so there is no energy addition (e.g., "heat of combustion") in the energy equation of the gas (3) or particle (6) phases. In a reacting cell, before combustion, the reactants EOS are used; after combustion, the products EOS are used.

In [16] we have shown that these components behave as calorically-perfect gases for $T < 3{,}500\,K$. Thus it is appropriate to fit them solely as a function of temperature. Piecewise quadratic functions were used to define the components *c*:

$$u_c(T) = a_c T^2 + b_c T + c_c \qquad (c = A, DP, Al, P_k) \tag{17}$$

The coefficient values a_c, b_c, c_c are listed in tables of Appendix B. For computational cells containing a mixture of components, the mixture energy also satisfies a quadratic form:

$$u_m(T) = \sum_c Y_c u_c = a_m T_m^2 + b_m T_m + c_m \tag{18}$$

where the mixture coefficients are defined by:

$$a_m = \sum_c Y_c a_c\ ,\ b_m = \sum_c Y_c b_c\ ,\ c_m = \sum_c Y_c c_c\ ,\ R_m = \sum_c Y_c R_c \tag{19}$$

Given the mixture specific internal energy, u_m, the mixture temperature can be evaluated by solving (18) for T_m yielding:

$$T_m = [-b_m + \sqrt{b_m^2 - 4a_m(c_m - u_m)}\,]/2a_m \tag{20}$$

For pure cells, the pressure of a component is calculated from the perfect gas relation:

$$p_c = \rho_c R_c T_c \tag{21}$$

or from the JWL function in the detonation products gases [16]:

$$p_{JWL}(v,T) = A\left(1 - \frac{\omega \cdot v_0}{R_1 \cdot v}\right)e^{-R_1 \cdot v/v_0} + B\left(1 - \frac{\omega \cdot v_0}{R_2 \cdot v}\right)e^{-R_2 \cdot v/v_0} + RT/v \tag{21}$$

where *v* is the specific volume ($v = 1/\rho$). Note in this formulation, the JWL function is valid both along the detonation products isentrope (terms with coefficients *A* and *B*) for small expansions, and off the isentrope (third term: the perfect gas law) for large expansions. Since the specific internal energy has a quadratic dependence on temperature (17,18), this formulation implicitly takes into account variations in the specific heat at constant volume: $C_V(T) = 2aT + b$. Clearly, this approach is more accurate than typical JWL models that assume that the specific heat of the detonation products is constant. In mixed cells, the pressure is calculated from the mixture temperature by the law of additive pressures [17]:

$$p_m = \sum_c p_c(V_m, T_m) \tag{22}$$

where $p_c(V_m, T_m)$ denotes the pressure that would be exerted by component *c* if it existed alone at the temperature and volume of the mixture.

NUMERICAL METHODS

The governing equations (1)-(6) and (14)-(16) are integrated with high-resolution upwind methods that are high-order generalizations of Godunov's method [18]. The algorithm for gas phase conservation laws is based on an efficient Riemann solver for gasdynamics first developed by Colella and Glaz [19] and Colella and Woodward [20] and extended to generalized conservation laws by Bell et al. [21] and to un-split upwind schemes by Colella [22]. The solver was modified to accommodate negative specific internal energies (*vid*. Fig. 3 and 4) associated with our thermodynamic formulation. To illustrate the properties of the solver, we have applied it to a one-dimensional shock tube problem, where detonation products gases are separated from air by a diaphragm with jump conditions of: $p_2 / p_1 = 10$ and $\rho_2 / \rho_1 = 8$. The numerical simulation used this solver and the quadratic equations of state for air and detonation products. Results are presented in Fig. 6. The solution agrees very well with the analytic solution, based on the JWL and Gilmore equations of state. Note in particular, the large values of negative internal energies in the detonation products and the smooth, monotonic transition of the specific internal energy profile across the contact surface. The algorithm for the particle phase conservation laws is based on a Riemann solver for two-phase flows as developed by Collins et al [23]. The boundary condition for the particle phase at a solid wall was elastic reflection (i.e., momentum reversal). Source terms in (1)-(6) and (14)-(16) are treated with Strang splitting methods. To sum up, in our approach the integrators are based on Riemann solvers; information propagates along characteristics at the correct wave speeds, and they incorporate nonlinear wave interactions within the cell during the time step. They include a limiting step (slope flattening) that automatically reduces the order of approximation in the neighborhood of discontinuities, while in smooth regions of the flow the scheme is second order in time and space.

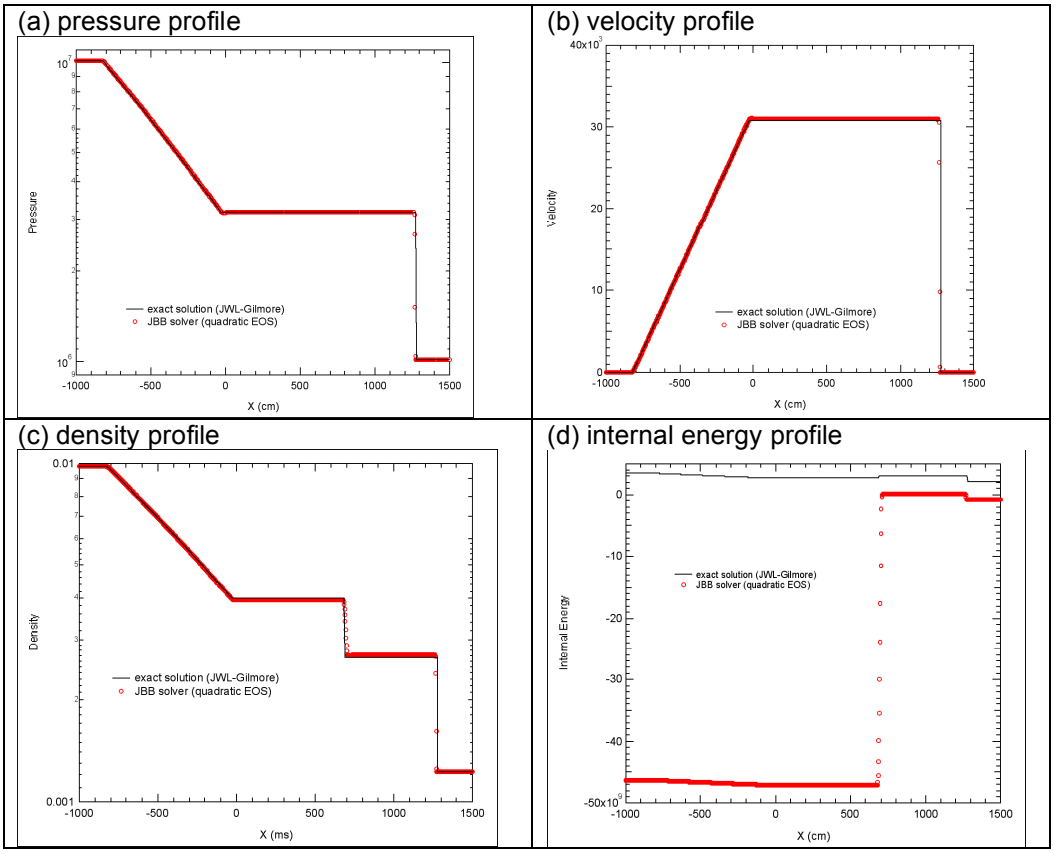

Figure 6. Solution of the shock tube problem ($p_2 / p_1 = 10$, $\rho_2 / \rho_1 = 8$) comparing the numerical solution based on the JBB solver (circles) with the exact solution (lines).

These Godunov schemes have been incorporated into an adaptive mesh refinement (AMR) algorithm that allows one to focus computational effort in complex regions of the flow such as mixing layers and reaction zones. Our adaptive methods are based on the block-structured AMR algorithms of Berger & Oliger [24] and Berger & Colella [25], and extended to three-dimensional hyperbolic systems by Bell et al. [26]. Embedded boundary methods are used to represent irregular geometries [27]. In this AMR approach, regions to be refined are organized into rectangular patches, with several hundred to several thousand grid-points per patch. One can refine on discontinuities (shocks and contact surfaces), on Richardson error estimates, or for present purposes, on flame surfaces and shocks. Grid patches are assigned to processors based on work-load estimates [28], so the AMR code runs efficiently on massively-parallel computers [29].

AMR is also used to refine turbulent mixing regions; by successive refinements we are able to capture the energy-bearing scales of the turbulence on the computational grid. In this way we are able to compute the effects of turbulent mixing without resorting to explicit turbulence modeling. This is consistent with the so-called MILES (Monotone Integrated Large-Eddy Simulation) approach of Boris [30]-[32]. A comprehensive review of implicit Large-Eddy Simulation (iLES) methods may be found in Grinstein et al [33]. A verification of the ability of our Godunov scheme to replicate the Kolmogorov spectrum of turbulent flows has been demonstrated by Aspden et al [34]. The scheme's ability to follow vorticity intensification during transition to turbulent flow is described by Bell and Marcus [35]. The scheme has also been used to predict transition in Kelvin-Helmholz shear layers; computed mean and second-moment profiles are found to be in good agreement with measured profiles [36].

RESULTS

CALORIMETER A

The 3D two-phase AMR code was used to simulate the explosion of a 1.5-g Al-SDF charge and the ensuing turbulent combustion with air in calorimeter A. Cross-sectional views of the temperature field at the mid-plane of the calorimeter (z = 10 cm) are presented in Fig. 7 at different times during the evolution of the combustion process. The PETN detonation products from the booster charge expand into the surrounding Al powder. They accelerate and heat the Al particles through drag and heat transfer. The products also mix with air in the powder and start afterburning; this ignites the Al particles, thereby initiating an Al-air combustion zone. By 30 μs, an expanding two-phase combustion shell has formed (see Fig. 7a). The particles have large radial velocities due to the intense initial drag acceleration by the gas. By 100 μs, they have become organized into fingers (radial striations), forming two-phase combustion jets (Fig. 7b). This is the two-phase analog to the mushroom-shaped combustion jets that form on the fuel-air interface during transition to turbulent combustion in gaseous systems [37]. The particle phase has no particle pressure, so it lacks a baroclynic mechanism ($\nabla p \times \nabla \rho$) to generate its own vorticity; therefore it cannot form rotational structures on the particle jet-air interface. Blast wave reflections from the chamber walls intensify mixing which promotes combustion. By 400 μs the combustion cloud fills the chamber and energy release proceeds in a distributed combustion mode (Fig. 7c). The fingering striations seen in the simulation at 100 μs were also observed in experiments (Fig. 7d). This illustrates that by using AMR, the simulation can capture the turbulent mixing structures on the computational grid.

Pressure histories associated with 1.5-g Al-SDF explosions in calorimeter A are presented in Figure 8; waveforms are shown both at early times and late times. The waveform from the numerical simulation (black curve) is quite similar to the measured waveform (red curve) out to 3 ms. Both curves are much larger than the waveform measured in a nitrogen atmosphere (blue curve)—thereby illustrating the dramatic effect that combustion has on the pressure field. Note that a 26.4 μs fiducial[3] was added to the computed waveform displayed in Fig. 8. The measured waveform at late times appears to be somewhat smoother than the numerical simulation; it seems that the experimental flow field was somewhat more dissipative than the numerical simulation. But overall, the energy release rate in the simulation must be similar to that in the experiment because the pressure histories agree.

[3] This is the *particle ignition delay*. This effect will be explored in the DISCUSSION section.

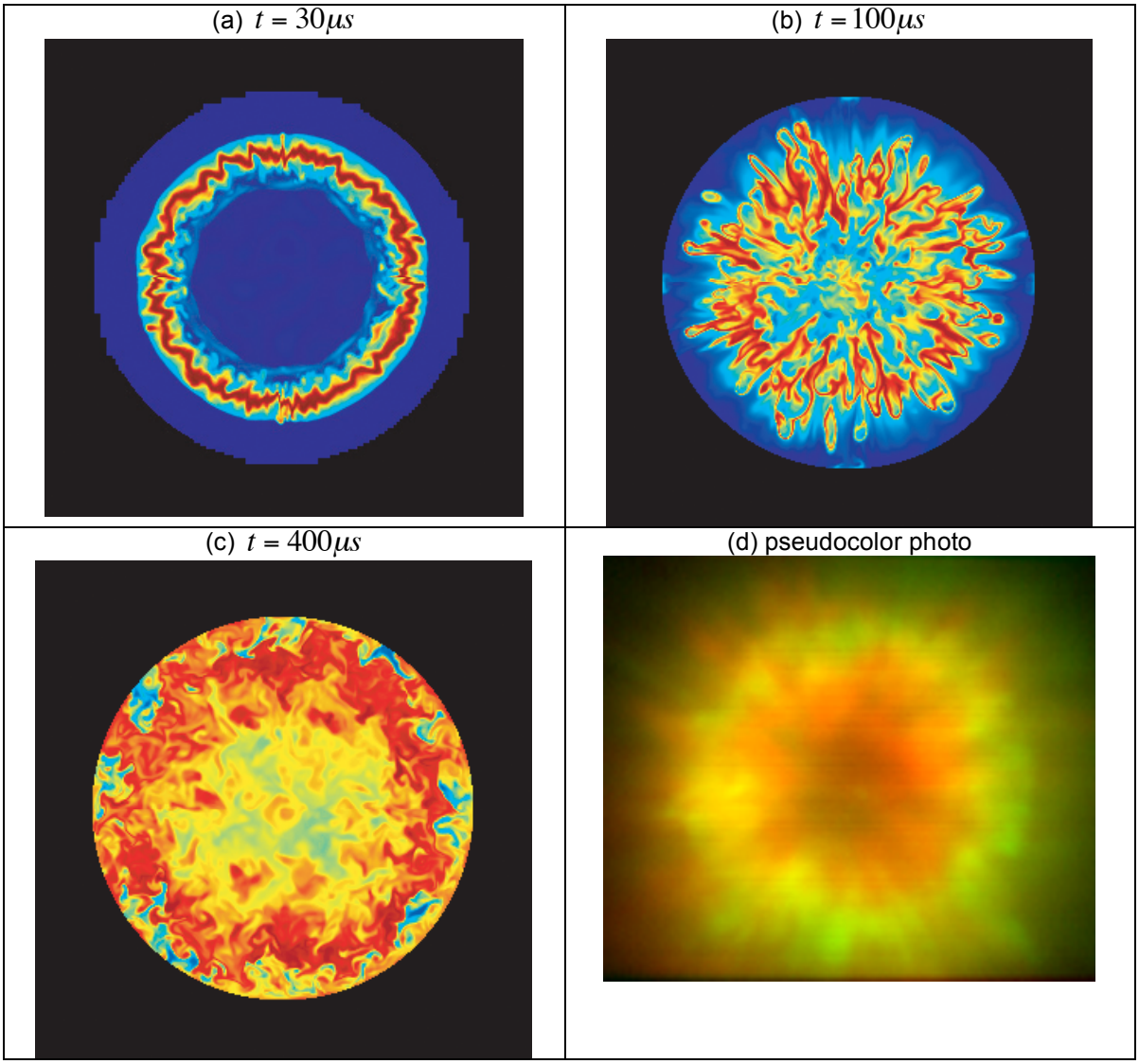

Figure 7. Cross-sectional view (z = 10 cm) of the temperature fields for the Al-air combustion cloud in calorimeter A.

(a) early-time waveforms

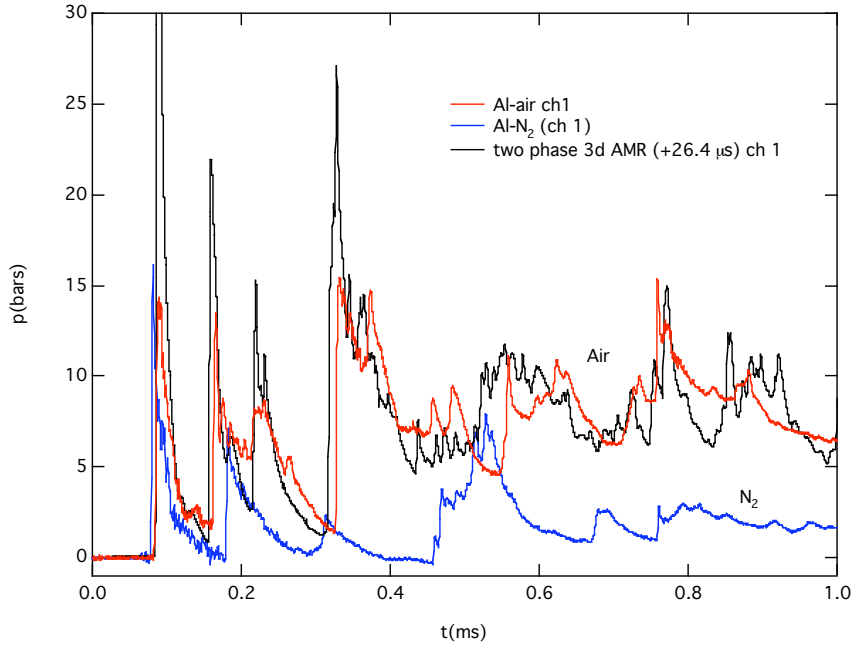

(b) late-time waveforms

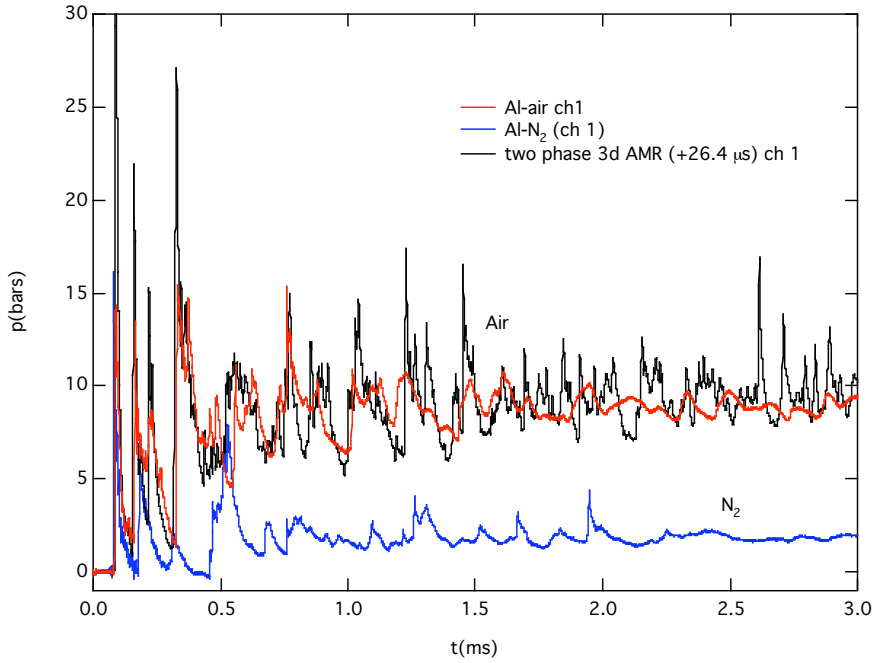

Figure 8. Pressure histories corresponding to 1.5-g Al-SDF charge explosion in the 6.6-liter calorimeter A: (a) early-time waveforms, (b) late-time waveforms (r = 5 cm, z = 10.5 cm).

CALORIMETER B

Next the AMR code was used to simulate the explosion of a 1.5-g Al-SDF charge in calorimeter B. Computed pressure histories at r = 5 cm on the chamber roof are compared with three gage records in Fig. 9. The waveform from the numerical simulation (black curve) is qualitatively similar to the measured waveform (red curve) out to a time of 1 ms. But the average of the computed waveform at 3 ms seems somewhat higher than the average of the three measured waveforms.

CALORIMETER C

Next the AMR code was used to simulate the explosion of a 1.5-g Al-SDF charge in calorimeter C. Computed pressure histories at r = 5 cm on the chamber roof are compared with four gage records in Fig. 10. The waveform from the numerical simulation (black curve) is qualitatively similar to the measured waveforms out to a time of 1 ms. But the average of the computed waveform at 3 ms seems somewhat higher than the average of the measured waveforms.

MASS HISTORIES

Evolution of the component masses from the numerical simulations of calorimeters A, B and C are presented in Figs. 11-13, respectively. There one can see that the Al particles are mostly depleted by 50μs —resulting in the formation of Al fuel, and the growth of combustion products of Al-air and PETN-air with time. One can also see the consumption of PETN detonation products starts at about 100 μs— producing PETN-air combustion products.

(a) early-time waveforms

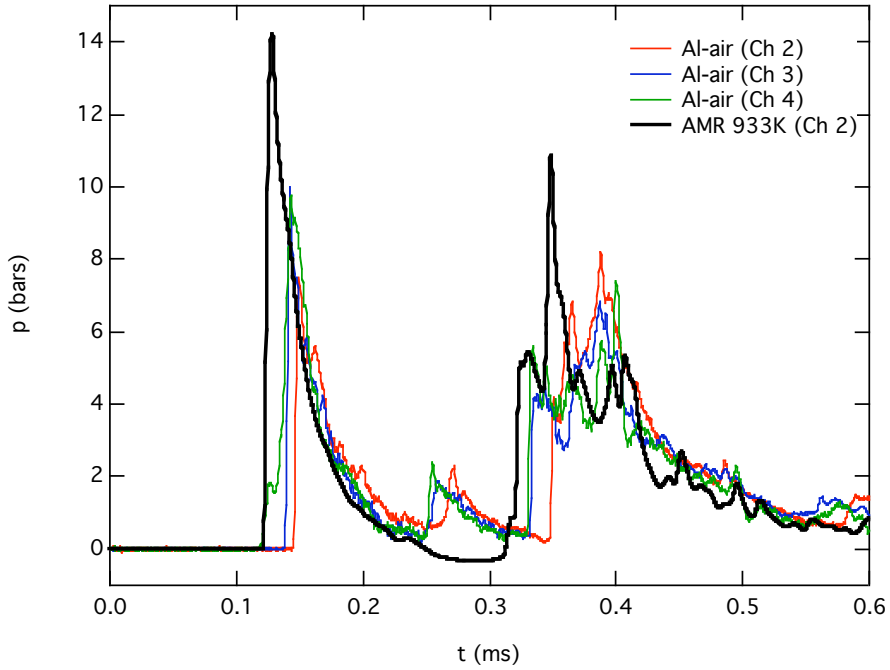

(b) late-time waveforms

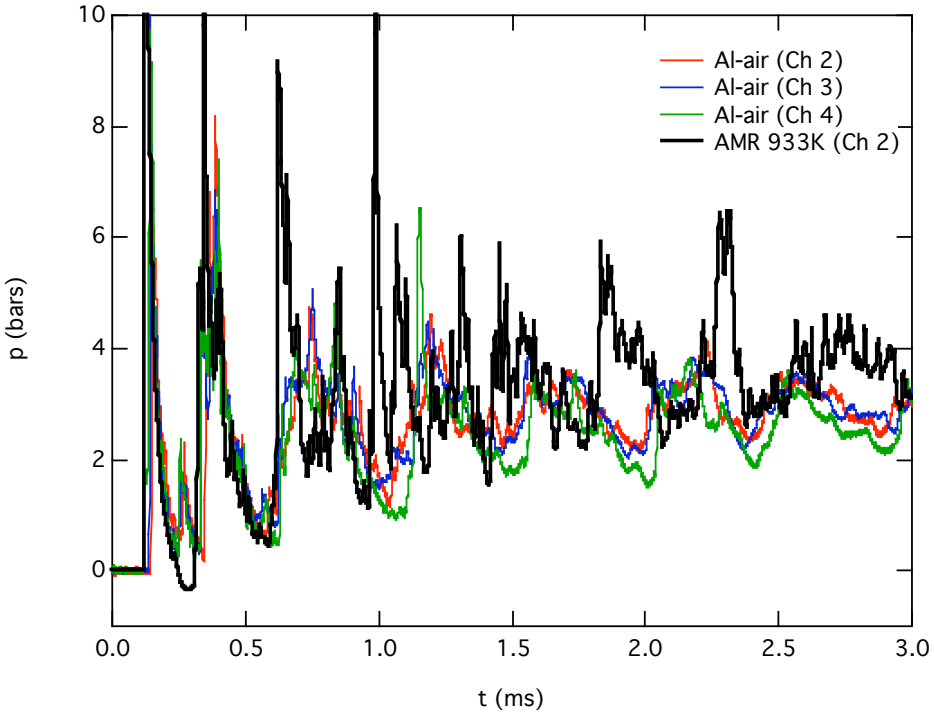

Figure 9. Pressure histories corresponding to 1.5-g Al-SDF charge explosion in the 21.2-liter calorimeter B: (a) early-time waveforms, (b) late-time waveforms (r = 5 cm, z = 15 cm).

(a) early-time waveforms

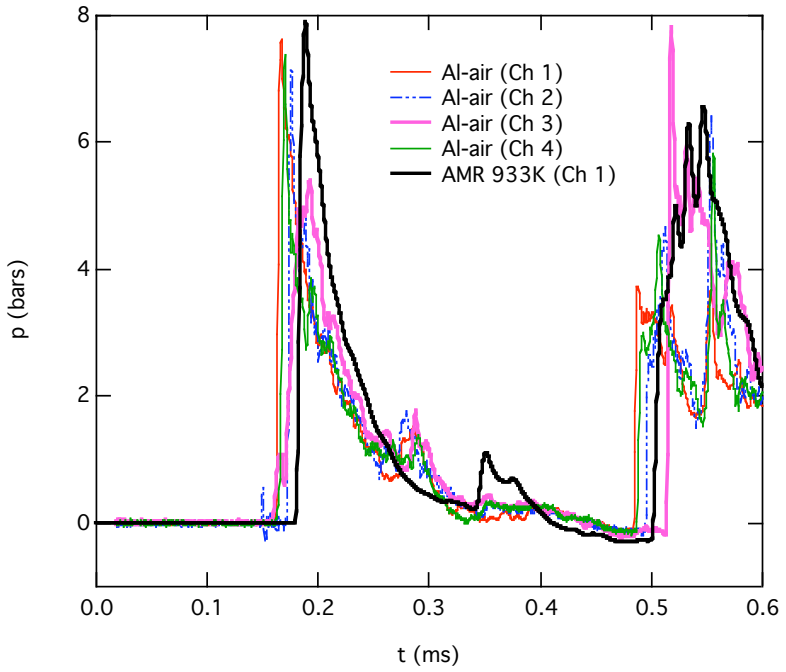

(b) late-time waveforms

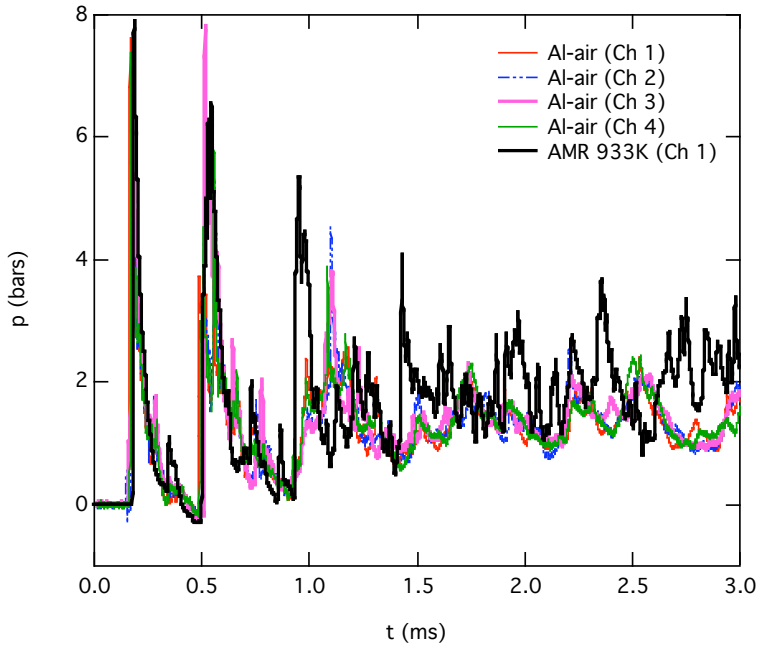

Figure 10. Pressure histories corresponding to 1.5-g Al-SDF charge explosion in 40.5-liter calorimeter C: (a) early-time waveforms, (b) late-time waveforms (r = 5 cm, z = 19 cm).

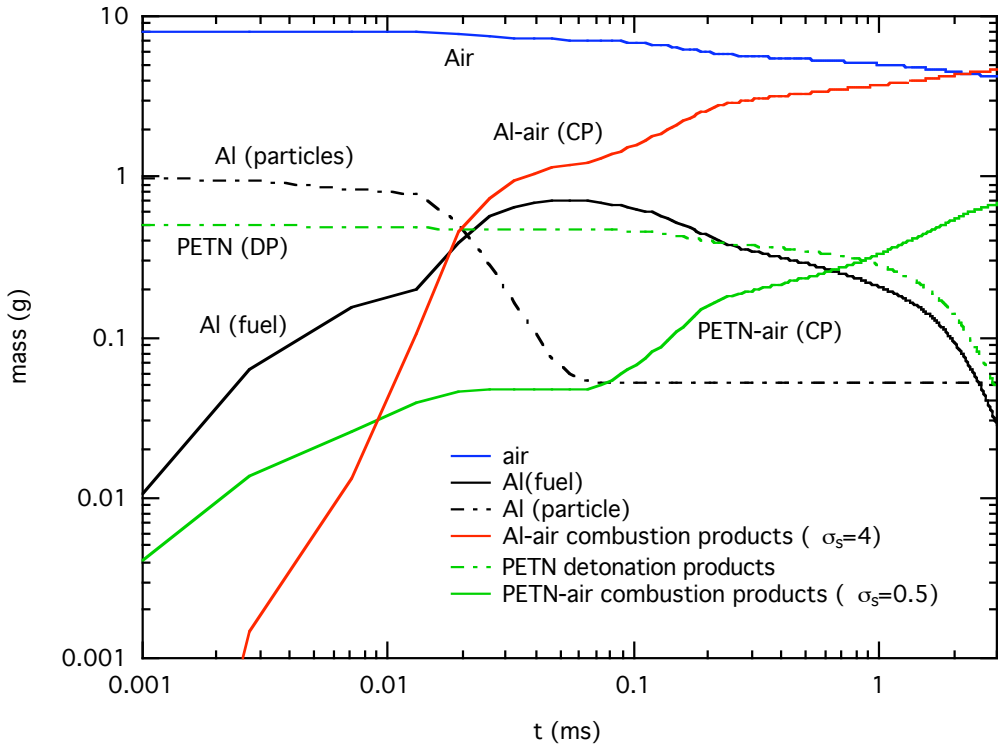

Figure 11. Evolution of component masses from the numerical simulation of combustion in calorimeter A.

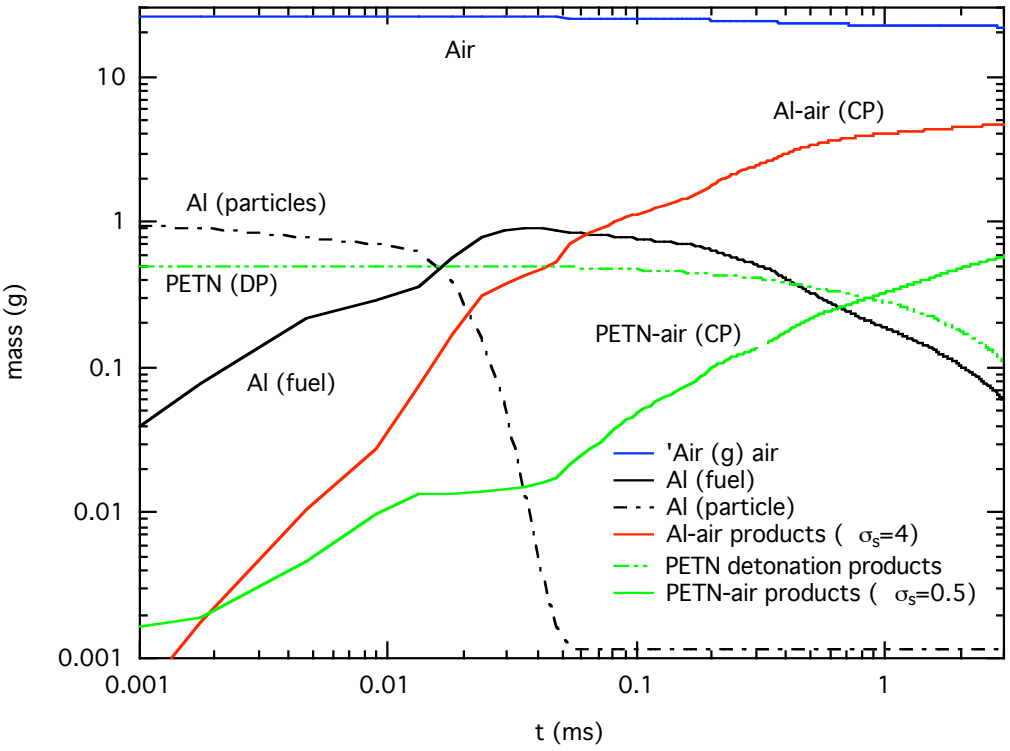

Figure 12. Evolution of component masses from the numerical simulation of combustion in calorimeter B.

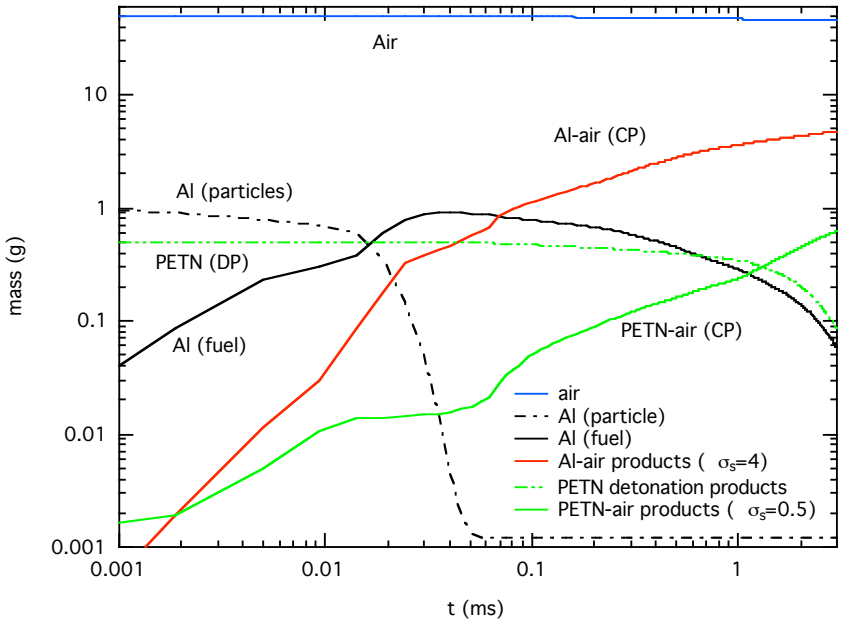

Figure 13. Evolution of component masses from the numerical simulation of combustion in calorimeter C.

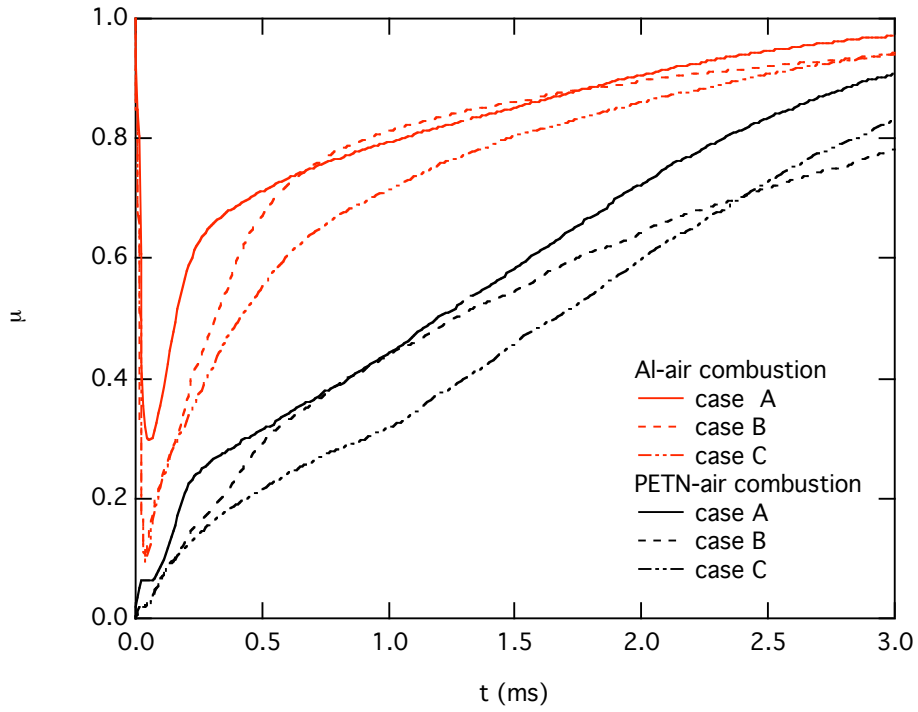

Figure 14. Evolution of mass-fraction of fuels (Al and PETN) consumed by combustion in calorimeters A, B and C.

FUEL CONSUMPTION

Figure 14 portrays evolution of the mass fraction of fuels: $\mu(t)$ consumed by combustion. The slope of the curves, $\dot{\mu}(t)$, represents the global burning rate. Burning rates are different for the different calorimeters because the turbulent mixing is influenced by the chamber geometry (e.g., distance to the chamber wall, chamber volume, etc.). However, by 3 ms in all cases, some 90-97% of the Al and some 80-90% of the PETN detonation products have been consumed by combustion with air. The computed results are compared with measurements in barometric calorimeters [1] in Table 1. These comparisons suggest that too much fuel was consumed in the numerical simulations—which showed up in excess pressure at 3 *ms*, as pointed out above (Figs. 9b and 10b). Measured fuel consumption was limited to 45-55%, for calorimeters C and B, respectively. We ascribe this to quenching effects in the experiment. In larger calorimeters, there is less reflected-shock heating of the air mass because the walls are farther away from the charge. When the relatively cooler air mass is entrained into the combustion cloud, it effectively reduces the gas temperature—thereby slowing (quenching) the chemical reactions.

Table 1. Fuel Consumption: Experiment versus Numerical Simulation

Calorimeter	Fuel Consumed (%)		Error (%)
	Experiment	AMR simulation @ 3 ms	
A	87.6 ± 1.4	97.1	+10%
B	55.0 ± 1.2	94.0	+39%
C	44.9 ± 1.8	94.2	+50%

DISCUSSION

The current combustion model assumes that the rate of production of combustion products is controlled solely by the rate that fuel and oxidizer are brought together by turbulent mixing. We call this the “fast-chemistry limit”. This mixing-limited combustion model worked successfully in simulating afterburning of TNT detonation products gases with air in six previous cases: 3 calorimetric chambers and 3 calorimetric tunnels [10].

However, in two-phase systems, ignition and combustion are controlled by physio-chemical interaction processes between phases. From a literature review, two characteristic ignition temperatures were identified:

$T_{ign} = 933 K$, based on the Al powder torch experiments of Gurevich et al. [38]

$T_{ign} = 1,785 K$, based on the thermal explosion model of Federov & Kharlamova [39]

An ignition temperature requirement: $T \geq T_{ign}$ was added to the combustion model, and numerical simulations of an SDF explosion in calorimeter B were repeated. The computed pressure histories are presented in Fig. 15. Adding the ignition temperature requirement delayed combustion, thereby delaying the arrival of the initial blast wave by 26 μs (the effective induction time for the particles); this was just enough to make it agree with the experimental shock arrival time. The computed waveforms also agree with the pressure measurements for the first and second blast waves, using either ignition-temperature criteria, whereas the simulation without an ignition criterion (dashed curve) is clearly different than the measured waveforms.

The computed pressure of the third blast wave (arriving at 0.62 ms) is higher than the data—indicating that there are additional physical effects limiting the temporal evolution of the combustion. One such effect is kinetics. The experiments of shock-induced ignition of aluminium particle clouds have been reported by Boiko et al [40, 41]. Measured ignition delays were fit with an Arrhenius function:

$$\tau_{ign} = a e^{E_a / RT} \tag{23}$$

The activation energy was $E_a = 60\,kCal/mole$ with a pre-exponential factor of $a = 1.6 \times 10^{-8}$ for aluminium flakes and $a = 2.5 \times 10^{-8}$ for 3-5 μs aluminium spheres. Assuming an ignition delay of 26 μs, the above relation implies an effective ignition temperature of 4,060 K for unsteady ignition of the flake aluminium cloud in the blast wave from an SDF explosion. This value is similar to the adiabatic flame temperature 4,120 K for stoichiometric Al-air combustion.

A collage of the cross-section temperature field at different times is presented in Fig. 16 from AMR simulations of an explosion in calorimeter B. It shows that at early times ($t < 83\,\mu s$), combustion occurs on the surface of the mixing fingers; one expects the combustion rate to be limited by the turbulent mixing rate. By 100 μs, the process has transitioned to a distributed combustion mode. Ballistic mixing of the Al particles with air has distributed oxidizer throughout the cloud, and one expects combustion to be limited/controlled by chemical kinetic rates.

The present formulation of the problem assumes that the system behaves as a dilute heterogeneous continuum, and indeed for most of the explosion time this is a valid approximation. However, during the initial dispersion phase, the Al particle cloud is compressed by the booster gases, causing dense continuum effects such as particle-particle collisions. In this regime, particle collisions create compaction-pressure effects that limit the compression of the particle phase. Also, the high density of particles leads to multi-particle drag effects which couple the fluid and particle phases more tightly. These effects are occurring during the ignition induction time of the particles, and may influence the ignition process. Such effects should be explored in the future using a dense heterogeneous continuum model.

RESUMÉ

A heterogeneous continuum model is proposed to describe the dispersion and combustion of an Al particle cloud in a confined explosion. It combines the gasdynamic conservation laws for the gas phase with a continuum formulation of a dilute particulate phase, as delineated by Nigmatulin. Inter-phase mass, momentum and energy exchange are prescribed by phenomenological laws of Khasainov. It incorporates a combustion model based on the mass conservation laws for fuel, air and products components; mass source/sink terms are treated in the fast-chemistry limit appropriate for such gasdynamic fields. The model takes into account both the afterburning of the booster detonation products with air, and the combustion of fuel (Al powder) with air. In this formulation, combustion becomes material transformations: *Reactants → Products at constant energy*. Note that in this approach, energy of the combustion system is constant, so there is no energy source (addition of the heat of combustion) in the gas-phase energy equation (3). Loci of component states in the $u - T$ plane are fit with piece-wise quadratic functions, thereby accurately defining the EOS for the components. The model equations are integrated with high-order Godunov schemes for both the gas and particle phases; source terms are treated with Strang splitting. Adaptive mesh refinement is used to capture the energy-bearing scales of the turbulence without resorting to turbulence modeling. The code runs efficiently on massively parallel computers; this capability is needed to capture effects of turbulent mixing on the grid.

(a) Ignition temperature model variations

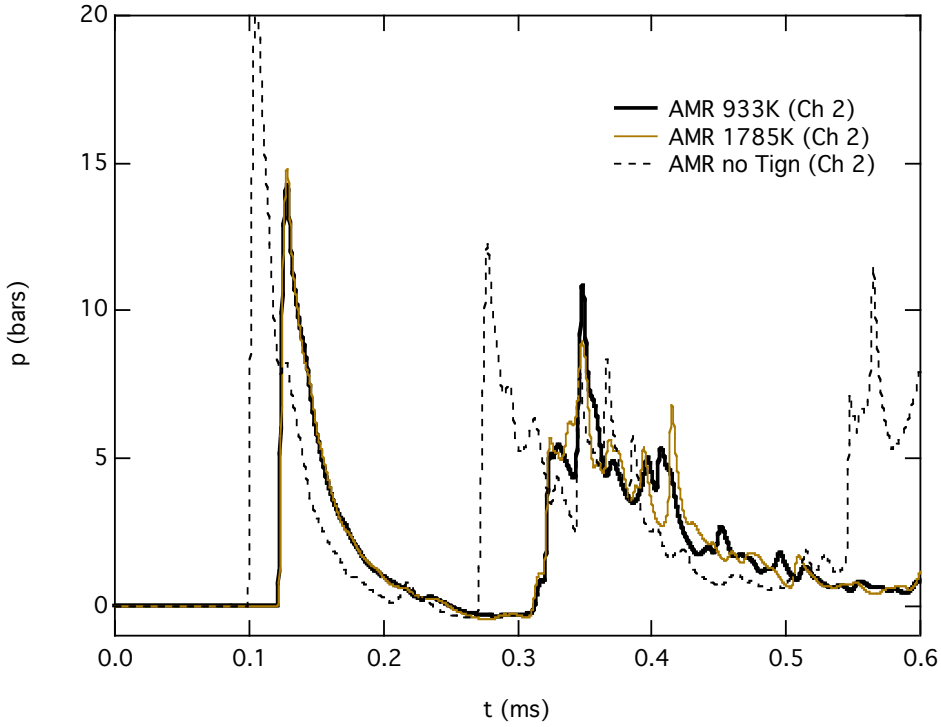

(b) Comparison with data

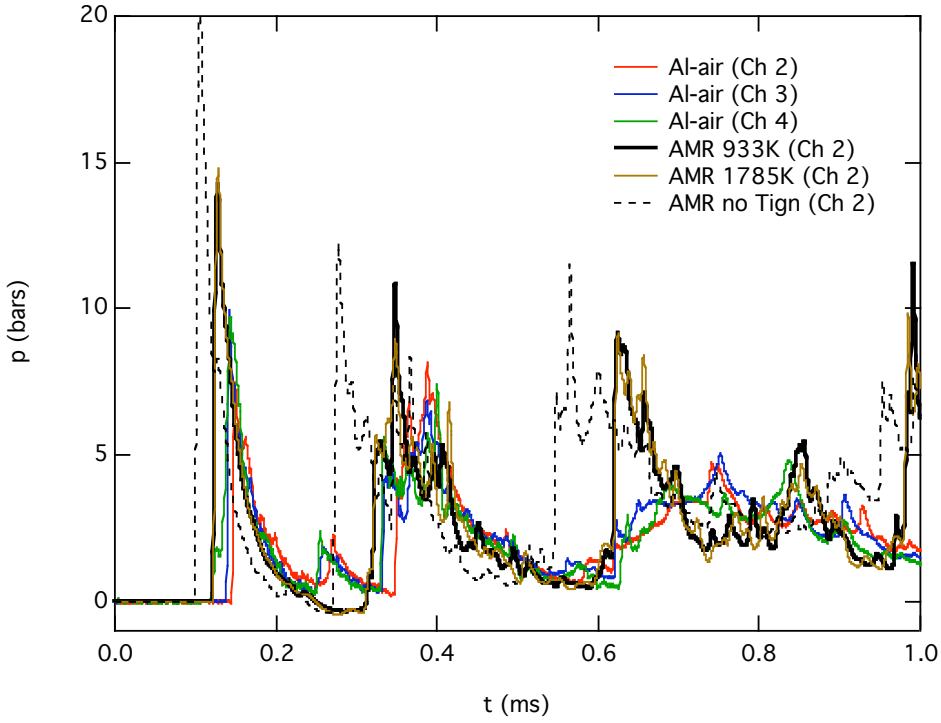

Figure 15. Comparison of computed pressure histories at r = 5 cm, z = 15 cm for calorimeter B, assuming an ignition temperature of 933K or 1785K versus no ignition criteria.

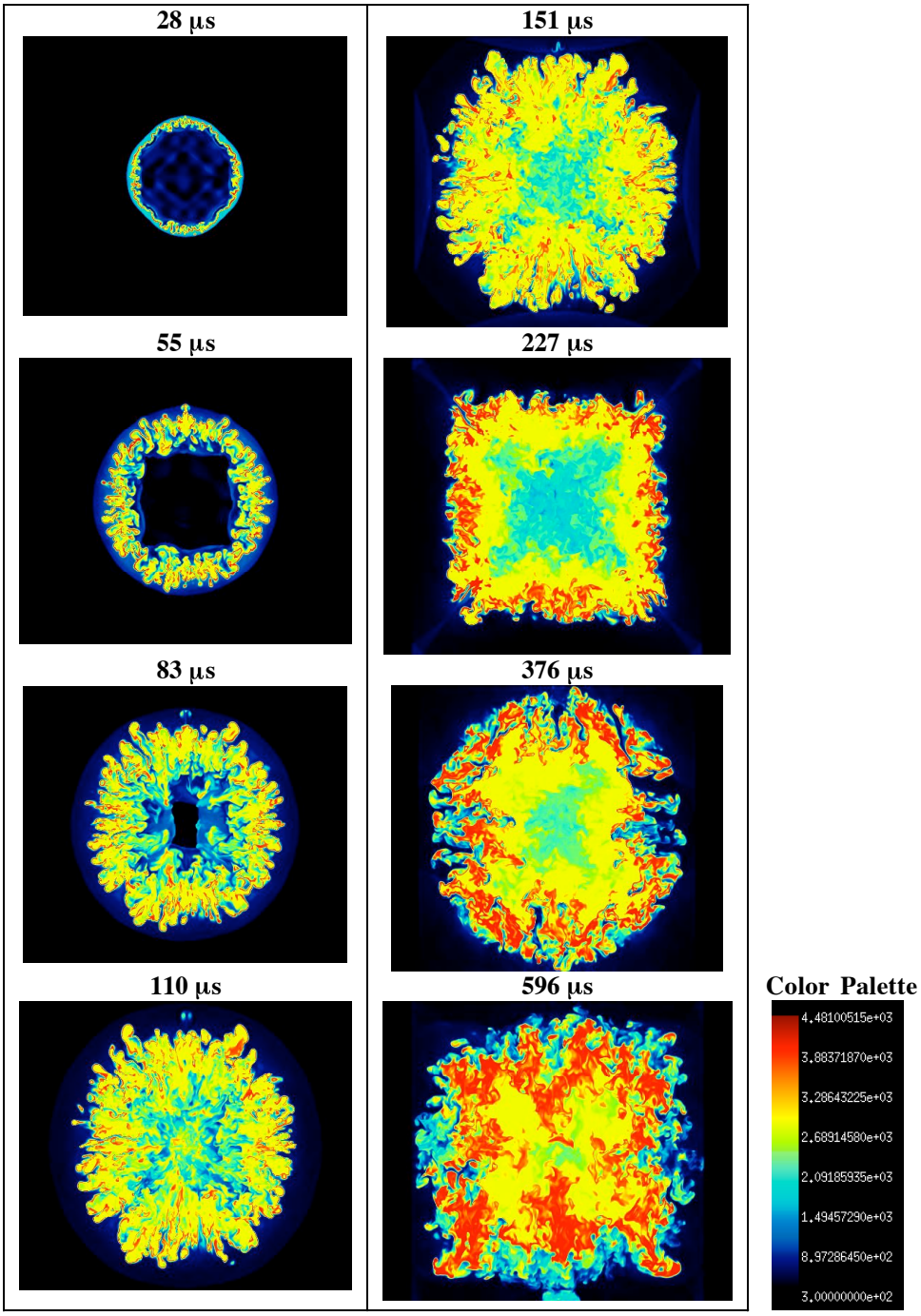

Figure 16. Vertical cross-section of temperature fields from the explosion of a 1.5-g Al-SDF charge in chamber B; see inset palette for temperature-color map: *blue* = 1,000 K, *turquoise* = 2,000 K, *yellow* = 3,000 K, *red* = 4,400 K.

CONCLUSIONS

The two-phase AMR code was used to simulate the explosion and combustion of 1.5-g Al-SDF charges in calorimeters with volumes of 6.6, 21.2 and 40.5 liters. Predicted pressure histories were qualitatively similar to measured waveforms. But to get good agreement with arrival times and waveforms of first and second blast waves, an ignition temperature criterion was added to the combustion model. Computed results were insensitive to the value of the ignition temperature, that is, computed waveforms were similar for $T_{ign} = 933 K$ and 1,785 *K*.

A particle ignition delay of 26.4 μs was inferred by comparing computed versus experimental shock arrival times at $r = 5cm$ in calorimeter A. Using this delay in an Arrhenius ignition model (A7), an effective ignition temperature of 4,060 *K* was evaluated. This value is essentially equal to the adiabatic flame temperature (4,120 *K*) for Al-air combustion. Apparently the SDF charge configuration provides an extremely strong ignition source (i.e., Al particle contact with the 3,175 *K* detonation products), compared to the ignition sources in the experiments of Gurevich and Boiko.

The burning rates were different for the different calorimeters because the turbulent mixing was influenced by the chamber geometry. By 3 ms in all numerical simulations, more than 80% of the fuel was consumed by combustion with air. However, measured fuel consumption was limited to 45-55%, (calorimeters C and B, respectively). We ascribe this difference to un-modeled effects (e.g., kinetics).

Ignition of aluminum particle clouds in SDF explosions involves an additional level of complexity due to the inherent non-steadiness of the problem. Ignition depends on more than just an ignition temperature. It depends on a competition between heating rates/power and cooling rates/power:

(i) the rate that particles are heated by the detonation products gases, ignite and consequently heat the surrounding gases by combustion, versus

(ii) the rate that the surrounding gases are cooled by blast wave expansion, radiation losses and entrainment of cooler air by turbulent mixing.

The fate of the Al particle cloud then depends on a collective competition of ignition over all scales of the particle ensemble distribution of the cloud. In future simulations, a kinetic ignition model will be added to explore such effects.

FUTURE WORK

Future work will explore physical effects that influence ignition of the Al particle cloud, including: (i) dense continuum effects (e.g., finite-particle-volume effects, particle-compaction pressures, and multi-particle drag effects), (ii) physical-chemical kinetics models, and (iii) statistical particle ignition modeling.

ACKNOWLEDGMENTS

This work was performed under the auspices of the U. S. Department of Energy by Lawrence Livermore National Laboratory under Contract No. DE-AC52-07NA27344. It was sponsored by the Defense Threat Reduction Agency under IACRO # 06-40731 and IACRO # 09-4509I.

REFERENCES

1. Kuhl, A. L. Barometric Calorimeters, *J. Physical Chemistry* B, 2009 (in press).
2. Kuhl, A. L. and Reichenbach, H. Combustion Effects in Confined Explosions, *Proceedings of the Combustion Institute* **32**, 2009, pp. 2291-2298.
3. Neuwald, P., Reichenbach, H. & Kuhl, A. L. Shock-Dispersed Fuel Charges—Combustion in Chambers and Tunnels, *Energetic Materials: Structure and Properties,* Thirty-fourth Int. Annual Conference of the Institut Chemische Technologie (ICT), 2003, pp. 13.1-13.14.
4. Neuwald, P. Reichenbach, H & Kuhl, A. L. Shock-Dispersed Flake Aluminum—Performance in Environments of Different Geometries, *Energetic Materials: Performance and Safety,* Thirty-sixth Int. Annual Conference of the Institut Chemische Technologie (ICT), 2005, pp. 71.1-71.12.
5. Neuwald, P., Reichenbach, H. & Kuhl, A. L. Combustion of Shock-Dispersed-Flake Aluminum—High-Speed Visualization, *Energetic Materials: Insensitivity, Ageing, Monitoring*, Thirty-seventh Int. Annual Conference of the Institut Chemische Technologie (ICT), 2006, pp. 116.1 to 116.12.
6. Reichenbach, H., Neuwald, P. & Kuhl, A. L., Waveforms Measured in Confined Thermobaric Explosions, *Energetic Materials: Characterisation and Preformance of Advanced Systems*, Thirty-eighth Int. Annual Conference of the Institut Chemische Technologie (ICT), 2007, pp. 3.1-3.11.
7. Kuhl, A. L., Neuwald, P. & Reichenbach, H., Effectiveness of Combustion of Shock-Dispersed Fuels in Calorimeters of Various Volumes, *Combustion, Explosion & Shock Waves*, **42** (6), 2006, pp. 731-734.
8. Kuhl, A.L. Thermodynamics of Combustion of TNT Products in a Chamber, ХИМИУЕСКАЯ ФИЗИКА 25:10, pp. 42-48.
9. Nigmatulin, R. I., ***Dynamics of Multi-phase Flows***, Vol 1. Moscow, Nauka, 1987, 464 pp.
10. Kuhl, A. L., Bell, J.B., Beckner, V. E., & Khasainov, B., Numerical Simulations of Thermobaric Explosions, *Energetic Materials: Characterization and Performance of Advanced Systems*, 38th Int. Annual Conf. of ICT, Fraunhofer Inst. Chemicsche Technologie (ICT), 2007, pp. 1.1-1.14.
11. Bell, J. B., Kuhl, A. L., & Beckner, V. E., Simulation of Enhanced-Explosive Devices in Chambers and Tunnels, *HPCMP Users Group Conference 2007*, 0-7695-3088-5/07, IEEE.
12. Khasainov, B., Kuhl, A. L., Victorov, S., Neuwald, P. Model of Non-Premixed Combustion of Al-Air Mixtures, *14th APS Meeting on Shock Compression Condensed in Matter*, AIP Proceedings **845**, part 1, 2005, pp. 449-452.
13. Ingignoli, W., *Etude de la formation et de la propagation des détonations dans des suspensions de particules d'aluminium en atmosphère oxydante ou réactive*. Thèse d'Université de Poitiers, France, 1999. 495 pp.
14. Veyssiere, B., and Khasainov, B. A Model for steady, Plane, Double-front Detonations (DFD) in Gaseous Explosive Mixtures with Aluminum Particles in Suspension, *Combustion and Flame*, Vol. **85** (1, 2), 1991, pp. 241-253.
15. Kobiera, A., Szymczyk, J., Wolanski, P. and Kuhl, A. L., Study of the Shock-Induced Acceleration of Hexane Droplets, *Shock Waves*, Vol. **18** (6), 2009, pp. 475.
16. Kuhl, A. L., Khasainov, B., Quadratic Model of Thermodynamic States in SDF Explosions, *Energetic Materials: Characterization and Performance of Advanced Systems*, Thirty-eighth Int. Annual Conference of the Institut Chemische Technologie (ICT), 2007, pp. 143.1-11.
17. Jones, J. B., and Hawkins, G. A. ***Engineering Thermodynamics: An Introductory Textbook***, Wiley, New York, 1960, p. 405.
18. van Leer, B. Towards the Ultimate Conservative Difference Scheme V: a Second-order Sequel to Godunov's Methods, *J Comp. Phys*., **32**, 1979, pp. 101-136.
19. Colella, P. & Glaz, H. M., Efficient Solution Algorithms for the Riemann Problem for Real Gases, *J Comp. Phys*., **59**, 1985, pp. 264-289.

20. Colella, P. & P. R. Woodward, P. R., The Piecewise Parabolic Method (PPM) for Gasdynamical Simulations, *J Comp. Phys*., **54,** 1984, pp. 174-201.

21. Bell, J. B., Colella, P. & Trangenstein, J. A., Higher Order Godunov Methods for General Systems of Hyperbolic Conservation Laws, *J Comp. Phys*., **92**(2), 1989, pp. 362-397.

22. Colella, P. Multidimensional Upwind Methods for Hyperbolic Conservation Laws, *J Comp. Phys*., **87**, 1990, pp. 171-200.

23. Collins, P., Ferguson, R. E., Chien, K-Y., Kuhl, A. L., Krispin, J. & Glaz, H. M., Simulation of Shock-Induced Dusty Gas Flows Using Various Models, *AIAA 94-2309*, AIAA Fluid Dynamics Conference, 1994.

24. Berger, J. M. & Oliger, J. Adaptive Mesh Refinement for Hyperbolic Partial Differential Equations, *J Comp. Phys*., **53**, 1984, pp. 484-512.

25. Berger, M. J. & Colella, P. Local Adaptive Mesh Refinement for Shock Hydrodynamics, *J Comp. Phys*., **82** (1), 1989, pp. 64-84.

26. Bell, J., Berger, J. M., Saltzman, J., & Welcome, M., A Three-dimensional Adaptive Mesh Refinement for Hyperbolic Conservation Laws, *SIAM J. Sci. Statist. Comput.,* **15**(1), 1994, pp. 127-138.

27. Pember, R. B., Bell, J. B., Colella, P., Crutchfield, W. Y., & Welcome, M. L., An Adaptive Cartesian Grid Method for Unsteady Compressible Flow in Complex Geometries, J Comp. Phys. 120 (2), 1995, pp. 278-304.

28. Crutchfield, W. Y., & Welcome, M. L., Object-Oriented Implementation of Adaptive Mesh Refinement Algorithms, *Scientific Programming*, **2**, 1993, pp. 145-156.

29. Rendleman, C. A., Beckner, V. E., Lijewski, M., Crutchfield, W. Y., & Bell, J. B., Parallelization of Structured, Hierarchical Adaptive Mesh Refinement Algorithms, *Computing and Visualization in Science,* Vol. **3**, 2000.

30. Boris, J. P., On Large Eddy Simulations Using Sub-Grid Turbulence Models, *Wither Turbulence? Turbulence at the Crossroads*, ed. J. L. Lumley, Lecture Notes in Physics, **257**, Springer-Verlag, Berlin, pp 344-353, 1989.

31. Boris, J. P., Grinstein, F. F., Oran, E. S., & Kolbe, R. L., New Insights into Large Eddy Simulation, *Fluid Dynamics Research*, **10**, pp. 199-228, 1992.

32. E. S. Oran, E. S. & Boris, J. P., **Numerical Simulation of Reactive Flow**, 2nd Ed., Cambridge University Press, Cambridge, UK, 529 pp, 2001 (vid. esp. § 12-4: Monotone-Integrated Large-Eddy Simulation, pp. 473-487).

33. Grinstein, F. F., Margolin, L. G., and Rider, W. J., Editors, **Implicit Large-Eddy Simulation: Computing Turbulent Fluid Dynamics**, Cambridge University Press, 546 pp., 2007.

34. Aspden, A. J., Nikiforakis, N, Dalziel, S. B. & Bell, J. B., Analysis of Implicit LES Methods, *Comm. Applied Mathematics and Computational Science*, **3,** pp.103-126, 2008.

35. Bell, J. B. & Marcus, D. L., Vorticity Intensification and Transition to Turbulence in the Three-Dimensional Euler Equations, *Comm. Math. Phys*. **147**, pp 371-394, 1992.

36. Chien, K.-Y., Ferguson, R. E., Kuhl, A. L., Glaz, H. M., Colella, P (1995) Inviscid Dynamics of Two-Dimensional Shear Layers, *Comp. Fluid Dynamics*, **5**, pp. 59-80, 1995.

37. Kuhl, A. L., Spherical Mixing Layers in Explosions, **Dynamics of Exothermicity**, J. R. Bowen Ed., Gordon and Breach, 1996, pp. 290-320 (+ 2 color plates).

38. M. A. Gurevich, K. I Lapinka, E. S Ozerov, Ignition Limits of Aluminum Particles, *Fizika Goreniya i Vzryva*, Vol. **6**, No. 2, pp. 172-175, 1970.

39. Federov, A. V. and Kharlamova, Yu. V., Ignition of an Aluminum Particle, *Combustion, Explosion and Shock Waves*, Vol. **39**, No. 5, pp. 544-547, 2003.

40. Boiko, V. M., Lotov, V. V. and Papyrin, A. N., Ignition of Gas Suspensions of Metallic Powders in Reflected Shock Waves, *Combustion, Explosion and Shock Waves*, Vol. **25**, No. 2, pp. 193-199, 1989 [Fizika goreniya I Vzryva, Vol. 25 No. 2, pp. 67-74, 1989].

41. Boiko, V. M. and Poplavski, S. V., Self-Ignition and Ignition of Al Powders in Shock Waves, *Shock Waves*, Vol. **11**, pp. 289-295, 2002.

42. Friedman, R. and Maček, A., *Combustion and Flame*, Vol. **6**, pp. 9-19, 1962.

43. Merzhanov, A. G., Thermal Theory of Metal Particle Ignition, *AIAA Journal*, **13**(2), pp. 209-214, 1975.

44. Pokhil, P. F., Belyaev, A. F., Frolov, Yu. V., Logachev, V. S. and Korotkov, A. I., **Combustion of Powdered Metals in Active Media** (in Russian), 1972 [FTD translation FTD-24-551-73, 395 pp, Foreign Technology Division, Air Force Systems Division, U. S. Air Force, reproduced by NTIS].

45. Korobeinikov, V. P., Levin, V. A., Markov, V. V. and Chernyi, G. G., Propagation of Blast Waves in a Combustible Gas, *Astonautic Acta*, Vol **17**, pp. 529-537, 1972.

46. Oran, E. S., Boris, J. P., Young, T. R., Flanigan, M. and Picone, M., **Simulation of gas phase detonations: introduction of an induction parameter model**, NRL Memorandum Report 4255, 1980.

47. Bird, R. B., Stewart, W. E., Lightfoot, E. N., **Transport Phenomena**, John Wiley, New York, 780 pp, 1960.

48. Hirschfelder, J. O., Curtiss, C. F. and Bird, R., B., **Molecular Theory of Liquids & Gases**, John Wiley, New York, 1219 pp, 1954.

49. **Handbook of Chemistry & Physics** (39th Ed.), C. D. Hodgman, R. C. Weast, S. M Selby, Editors, Chemical Rubber Publishing, Cleveland, Ohio, 3213 pp, 1958.

APPENDIX A

Transport Properties for Explosion Products Gases

The thermal conductivities (k_0) and viscosities (μ_0) of reactants, detonation products, and combustion products gases at $T = 0\,C$ and $p = 1\,atm$ are listed below[4]:

GAS	k_0(W/m-K)	μ_0(g/s-cm)
Air	0.0239	$1.716*10^{-4}$
N2	0.024	$1.75*10^{-4}$
CO	0.023	$1.70*10^{-4}$
CO2	0.0146	$1.46*10^{-4}$
$H2O_v$	0.0153	$1.27*10^{-4}$
H2	0.168	$0.83*10^{-4}$
DP	0.02096	$1.24*10^{-4}$ (mole-fraction weighted)
CP	0.0186	$1.53*10^{-4}$ (mole-fraction weighted)

Mole Fraction Composition of PETN

GAS	DP	CP
H2O	33%	26%
CO2	31%	33%
N2	6%	41%
CO	14%	0
H2	4%	0

Temperature Dependence

$$k(T) = k_0\sqrt{T/273} \tag{A1}$$

$$\mu(T) = \mu_0\sqrt{T/273} \tag{A2}$$

[4] basic data can be found in [47]-[49].

APPENDIX B
PIECE-WISE QUADRATIC EOS MODEL COEFFICIENTS

Table B1. Air EOS (10 bar)

Region *i*	a_A^i	b_A^i	c_A^i
1 (300—2,340K)	2.02768 E-5	0.16498	-71.9172
2 (2,340—3,700K)	1.34322 E-4	-0.41045	658.24424
3 (3,700—4,150K)	7.01281 E-5	0.11507	-403.36139
4 (4,150—4,530K)	-1.02084 E-4	1.53731	-3,340.674
5 (4,530—6,000K)	4.04923 E-5	0.11381	198.38643

Table B2. PETN detonation products EOS (CJ isentrope)

Region *i*	a_{DP}^i	b_{DP}^i	c_{DP}^i
1 (300—2,340K)	3.31674 E-5	0.20867	-1,890.164
2 (2,340—3,700K)	5.97088 E-5	0.0377	-1,634.868
3 (3,700—4,150K)	1.9052 E-4	-0.89226	20.04935
4 (4,150—4,530K)	2.28177 E-4	-1.20053	651.0422
5 (4,530—6,000K)	1.78281 E-4	-0.774255	-248.616

Table B3. PETN-air combustion products EOS (10 bars)

Region *i*	a_{CP}^i	b_{CP}^i	c_{CP}^i
1 (300—2,340K)	4.745 E-5	0.1549	-1,555.6
2 (2,340—3,700K)	4.6038 E-4	-1.7722	711.74
3 (3,700—4,150K)	4.9083 E-4	-1.841	558.87
4 (4,150—4,530K)	-6.1549 E-4	7.3463	-18,515.0
5 (4,530—6,000K)	-2.8216 E-4	3.8022	-9,254.5

Table B4. Al inert EOS

Region *i*	a_{Al}^i	b_{Al}^i	c_{Al}^i
1-5 (300—6,000K)	0	0.28128	-8.3895

Table B5. Al-Air combustion products EOS (10 bar)

Region *i*	a_P^i	b_P^i	c_P^i
1 (300—2,340K)	1.76153E-5	0.20186	-1,553.62
2 (2,340—3,700K)	1.49115 E-5	0.2502	-1,554.5182
3 (3,700—4,150K)	0.00113	-7.95255	13,553.8
4 (4,150—4,530K)	0.00826	-67.29752	137,084.51
5 (4,530—6,000K)	5.03544 E-5	-0.07059	1,216.0279

Table B6. Molecular mass for components

Component	condition	MW (g/mole)
Air	p=10 bars, $T < 3{,}000\,K$	28.85
PETN detonation products	isentrope, $T = 1{,}800\,K$	28.76
PETN-air combustion products ($\sigma_s = 0.482$)	p=10 bars, $T_a = 3{,}200\,K$	27.75
Al-air combustion products ($\sigma_s = 4.03$)	p=10bars, $T_a = 4{,}120\,K$	40.78